

Observations of magnetic reconnection in the deep solar atmosphere in the H ϵ line[★]

Luc H. M. Rouppe van der Voort^{1,2} , Jayant Joshi³ , and Kilian Krikova^{1,2} 

¹ Institute of Theoretical Astrophysics, University of Oslo, PO Box 1029 Blindern, 0315 Oslo, Norway
e-mail: rouppe@astro.uio.no

² Rosseland Centre for Solar Physics, University of Oslo, PO Box 1029 Blindern, 0315 Oslo, Norway

³ Indian Institute of Astrophysics, II Block, Koramangala, Bengaluru 560 034, India

Received 15 December 2023 / Accepted 21 January 2024

ABSTRACT

Context. Magnetic reconnection in the deep solar atmosphere can give rise to enhanced emission in the Balmer hydrogen lines, a phenomenon known as Ellerman bombs (EBs). It is most common to observe EBs in the H α and H β spectral lines. High-quality shorter-wavelength Balmer line observations of EBs are rare, but have the potential to provide the most highly resolved view on magnetic reconnection.

Aims. We aim to evaluate the H ϵ 3970 Å line as an EB diagnostic by analyzing high-quality observations in different Balmer lines.

Methods. Observations of different targets and viewing angles were acquired with the Swedish 1-m Solar Telescope. These observations sample EBs in different environments: active regions, the quiet Sun, and the penumbra and moat of a sunspot. We employed an automated detection method for quiet-Sun EBs based on *k*-means clustering.

Results. Ellerman bombs in the H ϵ line show similar characteristics as in the longer-wavelength Balmer lines: a higher intensity than in the surroundings, rapid variability, and a flame-like morphology. In a 24 min quiet-Sun time series, we detected 1674 EBs in the H ϵ line. This is 1.7 times more EBs than in H β . The quiet-Sun EBs measured in H ϵ are very similar to those in H β : They have similar lifetimes and a similar area, brightness, and spatial distribution. Most of the EBs detected in H ϵ are closer to the limb than their H β counterparts because the H ϵ line core EB emission is formed higher in the atmosphere than the H β EB wing emission.

Conclusions. We conclude that the H ϵ line is well suited for studying EBs, and consequently, for measuring the dynamics of magnetic reconnection in the solar atmosphere at the smallest scales. Our findings suggests that the deep atmosphere in the quiet Sun may host more than 750 000 reconnection events with an EB signature at any time. This is significantly more than what was found in earlier H β observations.

Key words. magnetic reconnection – Sun: activity – Sun: atmosphere – Sun: magnetic fields – sunspots

1. Introduction

The hydrogen Balmer lines can be used as a tracer of magnetic reconnection in the deep solar atmosphere. Enhanced emission in these spectral lines can be seen in sites where opposite magnetic polarities are in close proximity, flux cancellation is observed, and magnetic reconnection is thought to take place. The occurrence of concentrated sites with strong emission in the H α , H β , and H γ lines in active regions were first reported by Ellerman (1917) and the phenomenon is now commonly known as Ellerman bombs (EBs). The use of EB emission as a proxy for magnetic reconnection is supported by a vast body of observations in the current age of high-resolution solar observations (see, e.g., Georgoulis et al. 2002; Pariat et al. 2004, 2007; Fang et al. 2006; Matsumoto et al. 2008; Watanabe et al. 2008; Guglielmino et al. 2010; Reid et al. 2016).

The characteristic EB spectral profile has enhanced wings that appear in emission (with a peak emission in both wings around 40 km s⁻¹ Doppler offset) and line core absorption that has a similar low-intensity level as the surroundings. This profile is sometimes described as moustache-like (Severny 1964). The unperturbed line core is a sign that the site at which the

enhanced emission originates is situated below the chromospheric canopy of fibrils. This was confirmed in high-resolution imaging spectroscopy (Watanabe et al. 2011; Vissers et al. 2013; Rutten et al. 2013; Nelson et al. 2013). Under an inclined viewing angle, observing regions away from disk center, H α wing images show EBs as 1–2 mm bright upright flames that flicker rapidly on a timescale of seconds and are rooted in the deep photosphere (Watanabe et al. 2011; Rutten et al. 2013; Nelson et al. 2015). The rapid variability and flame substructure have been interpreted as a sign of fast reconnection and the formation of plasmoids (Rouppe van der Voort et al. 2023, 2017). Numerical simulations have reproduced the formation of typical EB spectral profiles from flame-like structures, which are regions with reconnection along upright thin current sheets that are rooted in intergranular lanes and extend throughout the low solar atmosphere (Hansteen et al. 2017, 2019; Danilovic 2017).

Ellerman bombs are most commonly observed in active regions with fast flow patterns that move magnetic fields, such as in emerging flux regions. High spatial resolution observations of tiny EB-like flames in the quiet Sun demonstrated that the EB phenomenon is not exclusive for active regions (Rouppe van der Voort et al. 2016; Nelson et al. 2017; Shetye et al. 2018; Bose et al. 2023). Recently, Joshi et al. (2020, hereafter Paper I) and Joshi & Rouppe van der Voort (2022,

* Movies are available at <https://www.aanda.org>

hereafter [Paper II](#)) found that quiet-Sun EBs (QSEBs) are much more ubiquitous in new high-quality $H\beta$ observations. The shorter-wavelength $H\beta$ line allows for a higher spatial resolution and contrast than $H\alpha$ and facilitates the detection of smaller and weaker EB events. In [Paper II](#), it was found that the width of half of the QSEBs in $H\beta$ is smaller than $0''.19$. It is very challenging to resolve this spatial scale in $H\alpha$. Their analysis suggested that about half a million QSEBs are present in the solar atmosphere at any time. High spatial resolution $H\beta$ observations of sunspots showed that penumbrae are filled with large numbers of EB flames ([Roupe van der Voort et al. 2021](#)). The high density of penumbral EBs (PEBs) suggests that magnetic reconnection is ubiquitous in the deep atmosphere of sunspot penumbrae.

The remarkably enhanced EB visibility in recent $H\beta$ observations raises the question whether shorter-wavelength Balmer lines show even finer detail and a higher EB occurrence in the solar atmosphere. The $H\epsilon$ line at 3970 \AA is only about 1.5 \AA from the Ca II H line core. Its vicinity to the strong Ca II H line has some advantages from an instrumentation point of view, but it also poses some challenges for interpretation. Recently, [Krikova et al. \(2023\)](#) presented a detailed study of the spectral line formation of $H\epsilon$. The $H\epsilon$ line is most often a weak absorption feature against the extended Ca II H wings and shows the reversed granulation intensity pattern that is formed a few hundred kilometers above the photosphere. This means that the $H\epsilon$ line core mostly reflects the Ca II H background radiation. However, [Krikova et al. \(2023\)](#) also presented observations of small regions in the quiet Sun with $H\epsilon$ in emission, indicating heating. Here, we present a systematic overview of high-quality observations of different targets to evaluate the $H\epsilon$ line as an EB diagnostic.

2. Observations

The observations were obtained with the CHROMIS and CRISP ([Scharmer et al. 2008](#)) imaging spectro(polari)meters at the Swedish 1-m Solar Telescope (SST, [Scharmer et al. 2003](#)) in August 2020. With CHROMIS, we cycled through a multiline program sampling the $H\beta$, Ca II H , and $H\epsilon$ spectral lines. The $H\beta$ line was sampled at 27 line positions, between $\pm 2.1 \text{ \AA}$, with 0.10 \AA steps between $\pm 1.0 \text{ \AA}$, and coarser in the outer wings, avoiding strong line blends. The CHROMIS transmission bandwidth at $H\beta$ is 0.10 \AA . The prefilter that was used for Ca II H has a center wavelength 3968.8 \AA and a bandwidth 4.1 \AA . It allows us to sample the $H\epsilon$ line at 3970.1 \AA (at about $+1.5 \text{ \AA}$ offset from the Ca II H line center). We sampled the Ca II H line at 29 line positions from -0.96 to $+2.40 \text{ \AA}$ with steps of 0.12 \AA . The CHROMIS transmission bandwidth at Ca II H is 0.12 \AA . At $+2.40 \text{ \AA}$, the prefilter transmission is about 50% of the peak transmission. With this program, we cover extreme $H\epsilon$ emission profiles out to about $+0.9 \text{ \AA}$ from the nominal $H\epsilon$ line center. Later in the observing campaign, from 13 August 2020, we added three line positions in the Ca II H blue wing (at -2.20 , -1.50 , and -1.30 \AA). These additional blue-wing positions allow a simple subtraction images with the $H\epsilon$ position in the Ca II H red wing, which effectively shows sites with enhanced emission or absorption in the $H\epsilon$ line. In addition to sampling the Ca II H line, a continuum position at 4001 \AA was observed. This required a different CHROMIS prefilter, but was observed with the same wide-band (WB) filter as for Ca II H (center wavelength 3950 \AA and bandwidth 13.2 \AA). For $H\beta$ the WB filter had a center wavelength 4846 \AA and a bandwidth

6.5 \AA . Both WB channels effectively sample the photosphere. The temporal cadence of the CHROMIS observations was about 17 s (18 s from 13 August 2020). CHROMIS has a pixel scale of $0''.038$ and a field of view (FOV) of $66'' \times 42''$.

With CRISP, we sampled the $H\alpha$, $\text{Fe I } 6173 \text{ \AA}$, and $\text{Ca II } 8542 \text{ \AA}$ spectral lines at a cadence of 40 s . CRISP sampled the $H\alpha$ line at 31 line positions between $\pm 1.5 \text{ \AA}$ with 0.1 \AA steps. The $\text{Fe I } 6173 \text{ \AA}$ line was observed with polarimetry and was sampled at 13 line positions (between $\pm 0.16 \text{ \AA}$ with 0.04 \AA steps, and also at $\pm 0.24 \text{ \AA}$ and $\pm 0.32 \text{ \AA}$) plus the continuum at $+0.68 \text{ \AA}$ from the nominal line core. For each line position and polarization state, 8 exposures were acquired that were used for image restoration (i.e., a total of 448 exposures per spectral line scan). The noise level in the restored Stokes V/I_{cont} maps was estimated to be 2×10^{-3} . Furthermore, spectropolarimetric observations were acquired in the $\text{Ca II } 8542 \text{ \AA}$ line at 20 line positions between -1.68 and $+2.38 \text{ \AA}$. Maps of the magnetic field strength along the line of sight (B_{LOS}) were derived from Milne–Eddington inversions of the $\text{Fe I } 6173 \text{ \AA}$ observations using the inversion code developed by [de la Cruz Rodríguez \(2019\)](#). We estimate the noise level in the B_{LOS} maps to be 6 G . This was measured as the standard deviation in a very quiet region in the quiet-Sun time series on 16 August 2020.

The data were processed from raw exposures to science-ready data cubes using the SSTRED reduction pipeline ([de la Cruz Rodríguez et al. 2015](#); [Löfdahl et al. 2021](#)). An important step in the processing pipeline is the application of image restoration with the multi-object multiframe blind deconvolution (MOMFBD, [van Noort et al. 2005](#)) method. Each of the CRISP spectral lines and CHROMIS $H\beta$ data were processed separately, while $H\epsilon$ and the 4000 \AA continuum were processed together with Ca II H (the data were effectively separated by their respective filters in the WB channel). One of the final steps in the pipeline was alignment between the spectral line data cubes. This was done by cross-correlating the WB channels that showed similar photospheric scenes. The CHROMIS FOV and temporal cadence served as reference to which the lower-resolution CRISP data (pixel scale $0''.058$) were matched in space (the CRISP FOV is about $59'' \times 59''$) by linear interpolation and in time by nearest-neighbor sampling. The alignment of the data included destretching to account for residual seeing-induced image deformation that was not accounted for by the image restoration.

The details of the different data sets are provided in [Table 1](#). This includes measurements of the seeing quality in terms of the Fried parameter r_0 as provided by the SST adaptive optics wavefront sensor (see [Scharmer et al. 2019](#)). A high spatial resolution is required to resolve the smallest EBs and the fine structure in the larger EBs. We therefore selected spectral scans and time sequences during the best seeing conditions from the multiday observing campaign.

For a detailed comparison between QSEBs in $H\beta$ and $H\epsilon$, we selected a 24 min time series from the 16 August 2020 observation at $\mu = 0.54$ (81 time steps). The seeing was very good and stable during the full duration of the series, with only one time step with $r_0 = 8 \text{ cm}$ and 92% of the time steps $r_0 > 15 \text{ cm}$ (ground-layer seeing). For the full atmosphere seeing, $r_0 > 8 \text{ cm}$ for 93% of the time.

3. Methods

To gather statistics from the 24 min time series, we used an automated detection method to identify and track QSEBs. To identify

Table 1. Overview of the data sets.

Date	Time (UTC)	Target	(X, Y) ["]	μ	r_0 [cm]	Figure
2020-08-07	13:02:09	AR12770	(-412, 285)	0.85	29 (21)	3
2020-08-11	09:28:04	AR12770	(318, 295)	0.89	23 (10)	1
	09:23:24–09:39:02				33 (11)	1 (movie)
2020-08-13	07:58:51	AR	(-750, -502)	0.32	26 (9)	2
2020-08-15	09:00:26	CH	(0, 830)	0.49	44 (12)	2
2020-08-16	08:32:20–08:36:10	QS	(515, 619)	0.54	45 (12)	4
	08:17:01–08:41:12				51 (13)	5–10

Notes. Target types: active region (AR), coronal hole (CH), or quiet Sun (QS). (X, Y): approximate pointing coordinates. $\mu = \cos \theta$ with θ the observing angle. r_0 : maximum value of the Fried parameter for the ground-layer seeing. The value in parentheses covers both ground-layer and high-altitude seeing. The last column shows the figures for which the different data sets are used.

the spectral signatures of QSEBs in the $H\beta$ and $H\epsilon$ spectral data, we used the k -means clustering algorithm (Everitt 1972). In particular, we used the k -means++ (Arthur & Vassilvskii 2007) implementation in scikit-learn, which employs an optimized method for initialization. The basics of the methods are discussed in detail in Paper II and we concentrate here on some of the differences in the methods we employed here.

Before performing the k -means clustering, we normalized the $H\beta$ profiles by the average of the far-wing intensities. Then we applied a principle component analysis (PCA) to reduce the dimensionality of the $H\beta$ data set. The first ten PCA components explain 90% of the total variability in the data set, and these first ten components were further used for the k -means clustering. We clustered the PCA-manipulated $H\beta$ data into 100 groups ($k = 100$). While the k -means clustering was performed on the PCA-manipulated data, representative profiles (RPs) corresponding to each cluster were calculated from the original $H\beta$ profiles. We found 15 out of the 100 RPs with QSEB-like spectral signatures. These RPs are shown in Fig. A.1. For a detailed discussion of using PCA preprocessing before k -means clustering, we refer to Faber (2022), for instance.

While the fully observed spectral range was used for the clustering of the $H\beta$ profiles, for the k -means clustering in $H\epsilon$ we concentrated on the 13 spectral positions around the $H\epsilon$ line center, from -0.54 to $+0.90$ Å. Prior to k -means clustering, we normalized by the intensity level of the Ca II H blue-wing position at -1.5 Å. We identified 25 of the 100 clusters ($k = 100$) with $H\epsilon$ QSEB profiles. They are shown in Fig. A.2.

We selected 10 of the 81 time steps with good seeing conditions to train the $H\beta$ and $H\epsilon$ k -means models. In addition to these selected time steps, we incorporated pixels exhibiting potential QSEB signatures from the entire time series. These pixels were included by intensity thresholds, and during the training of the k -means models, they were assigned a weight four times higher than for the pixels from the ten best scans. The derived models were used to predict the closest RP for each pixel in the complete time series.

To detect QSEB events in the different time steps and track them over time, we closely followed the methods described in Paper II. This includes the three-dimensional (3D) morphological closing operation method to connect pixel areas with QSEB RPs and 3D connected component labeling (Fiorio & Gustedt 1996) to uniquely label events that are connected in space and time. We excluded events with lifetimes shorter than two time steps (36 s) and maximum areas smaller than five pixels. This means that both single-time step large events and small events living longer than two time steps were considered as genuine QSEBs. Some QSEB detections in one spectral line were close

in space and time to a detection in the other line and can be regarded as a single event detected in both lines. We consider an QSEB event as connected across the two spectral lines when the spatial offset and the temporal gap between their respective counterparts are smaller than 500 km and 162 s (see the Appendix for a more detailed discussion of connecting events).

4. Results

4.1. Ellerman bomb characteristics in $H\epsilon$

Figure 1 presents a strong EB in an active region. It is a fine example of an EB observation that displays many of the typical EB characteristics: Strong $H\alpha$ wing emission that is visible in the wing as a compact brightening of about 1" size, but is covered by chromospheric fibrils in the line core, which occurs at the interface between opposite-polarity magnetic field patches and is invisible in the 4001 Å continuum channel. The accompanying movie shows almost the full ~ 15 min lifetime of the event. The EB displays rapid variability during the event. The intensity signal in the $H\beta$ wing is strongly enhanced and varies from one frame to the next. The morphology simultaneously changes rapidly. Some thin linear extensions appear to emerge from the EB site, sometimes with detaching blob-like brightenings. This morphology is compatible with the flickering flame-like behavior that can be observed for EBs at a more slanted view farther toward the limb (this AR was observed with $\mu = 0.89$).

This event is associated with a magnetic flux emergence in which the emerging negative polarity crashed into preexisting positive-polarity concentrations. The emergence of the magnetic flux was accompanied with elongated so-called anomalous granulation. This can be best viewed in the movie associated with Fig. 4 in Roupe van der Voort et al. (2023), which was made from this observation.

The two $H\alpha$ and $H\beta$ spectral profiles in Fig. 1 show a classic EB profile with strong enhanced wings. The $H\epsilon$ line is also strongly enhanced. The $H\epsilon$ line center itself appears to be in absorption against enhanced $H\epsilon$ wings. It is difficult to distinguish the $H\epsilon$ line profile from the Ca II H profile, however. The Ca II H line itself is enhanced as well, with an enhanced H_3 line center and enhanced H_2 peaks as compared to the reference profile. The limited coverage of the Ca II H blue wing for this observation makes it difficult to see to which extent the $H\epsilon$ line is enhanced against the far Ca II H wings. In any case, the morphology of the EB in $H\epsilon$ blue wing is very similar to the corresponding $H\alpha$ and $H\beta$ blue-wing images. This is also clear from the associated movie, which shows that the EB evolution in the $H\epsilon$ blue wing is almost identical to that in the $H\beta$ blue wing. The

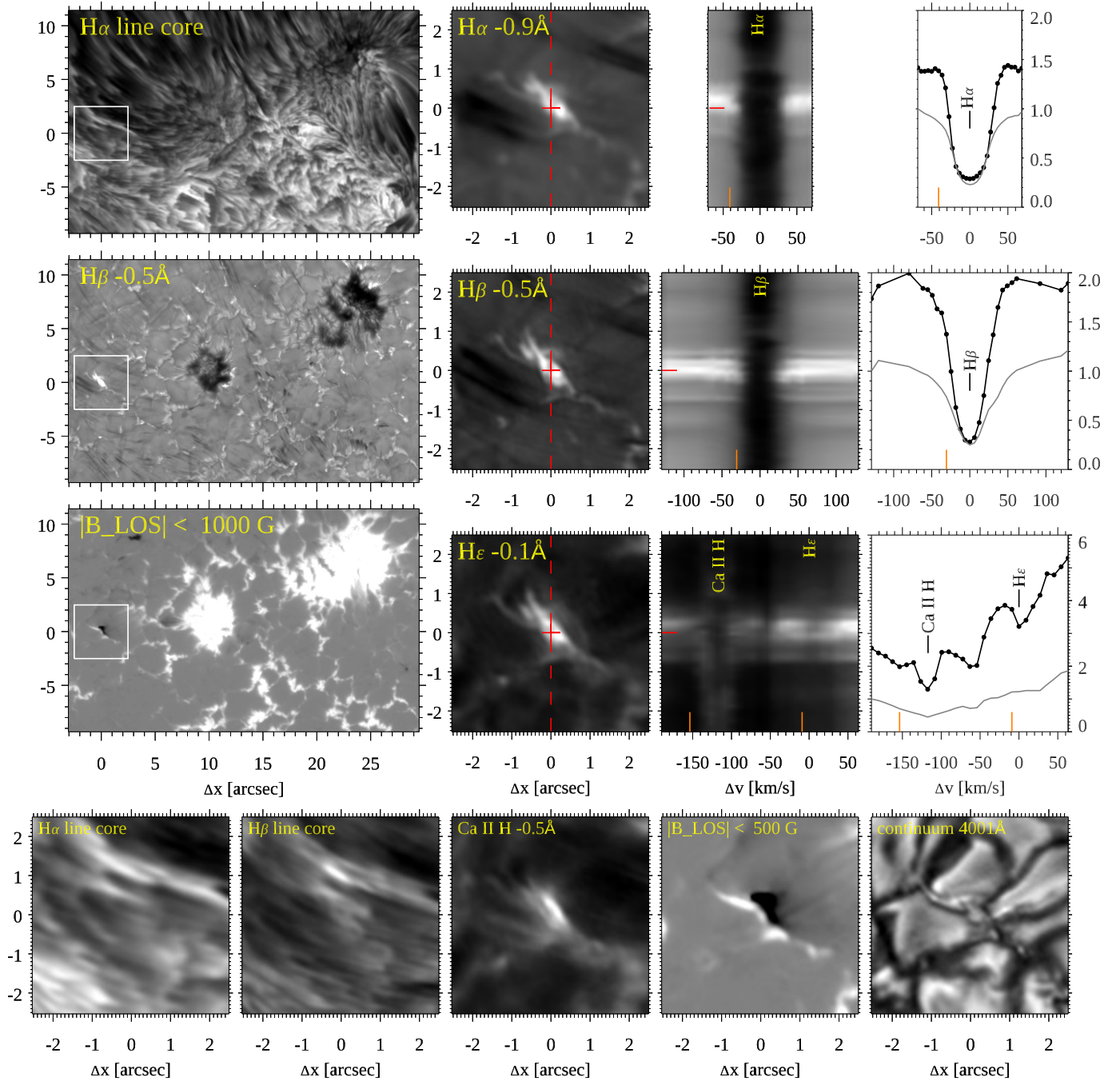


Fig. 1. Strong EB in an active region observed on 11 August 2020. The larger rectangular panels left in the top three rows show the larger context area in the $H\alpha$ line core, the $H\beta$ blue wing, and a magnetogram. The white square is centered on the EB and marks the area that is shown at larger magnification in the other square images. The dashed red line in the Balmer blue-wing images ($H\alpha$, $H\beta$, $H\epsilon$) marks the artificial slit for which the corresponding spectrogram (λ diagram) is shown to the right. The EB spectral profiles, marked by horizontal red dashes, are shown in the right panels as solid black lines with the observed sampling points marked as small filled circles. The thin gray profiles are reference spectral profiles averaged over the full region shown in the left context images. The vertical orange dashes mark the wavelength positions of the Balmer-wing images and the Ca II H blue-wing image in the bottom row. Two animations are available [online](#): one showing the temporal evolution of the middle rows of this figure, and one showing spectral line scans of the top three rows.

morphology of the EB in Ca II H blue wing is slightly different, but there is a clear bright linear feature at the EB site.

Figure 2 shows two examples of EBs in magnetically less active areas. The examples lie farther toward the limb than the EB in Fig. 1, and the apparent upright flame morphology is clear. In both examples, the flames appear to be aligned in the limb direction. The top example shows a tall EB flame in a

small active region that has an apparent length of more than $1''.7$ in $H\beta$ wing. This corresponds to a geometric length of more than 1300 km assuming a strictly vertical structure and taking the slanted viewing angle into account. The bottom example is a QSEB with an apparent length of about $0''.7$ (corresponding to an almost 600 km tall vertical structure). The two EBs are clearly visible in the $H\beta$ and $H\epsilon$ wing images and have a similar

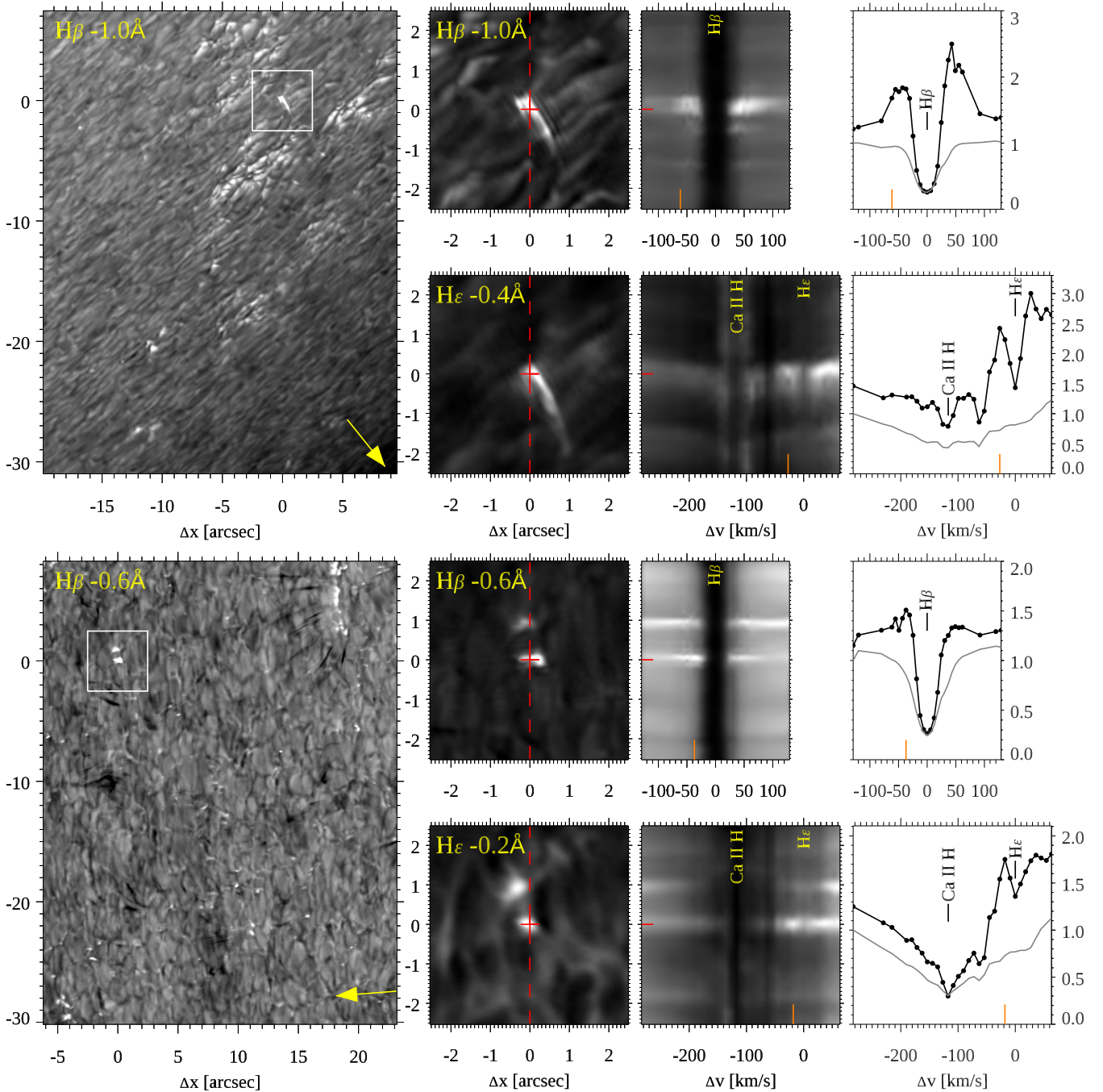


Fig. 2. Examples of EBs in a small active region (top, 13 August 2020) and in the quiet Sun (bottom, 15 August 2020). Both examples are close to the limb (top: $\mu = 0.32$, bottom: $\mu = 0.49$). The small white square in the overview images (left) are centered on the EBs shown at larger magnification in the $H\beta$ and $H\epsilon$ wing images in the next column. The yellow arrow in the lower-right corner of the overview image shows the direction toward the closest limb. The $\Delta\lambda$ spectrogram is shown for the vertical dashed red line in the center of the wing images and crosses the EB. The spectral profiles are shown for the center position, which is marked with the short horizontal red dash in the spectrogram. The thin gray profiles are reference spectral profiles averaged over the full region shown in the left context images. Animations that show the full spectral line scans of the two examples are available [online](#).

morphology in both lines. In the bottom example, another QSEB lies about $1''$ above the QSEB in the center. It appears to be largest in the $H\epsilon$ wing image. For these observations, we sampled more of the Ca II H blue wing, which highlights that the $H\epsilon$ line has a higher intensity than the Ca II H wing. Both examples have a pronounced central absorption at $H\epsilon$ line center.

From close inspection of the zoomed wing images in Fig. 2, a subtle spatial offset of the EBs between the two spectral lines is

visible: The EB in $H\epsilon$ is slightly offset in the direction toward the limb. For the tall flame in the active region in the top example, the red cross is centered on the base of the EB in $H\epsilon$, while the corresponding EB base in $H\beta$ wing is a few $0''.1$ towards the top left. The same can be seen for the two QSEBs in the bottom example: The QSEB brightenings in $H\epsilon$ are slightly shifted to the left, in the direction toward the limb. The spatial offset for QSEBs in the two lines is analyzed in more detail below.

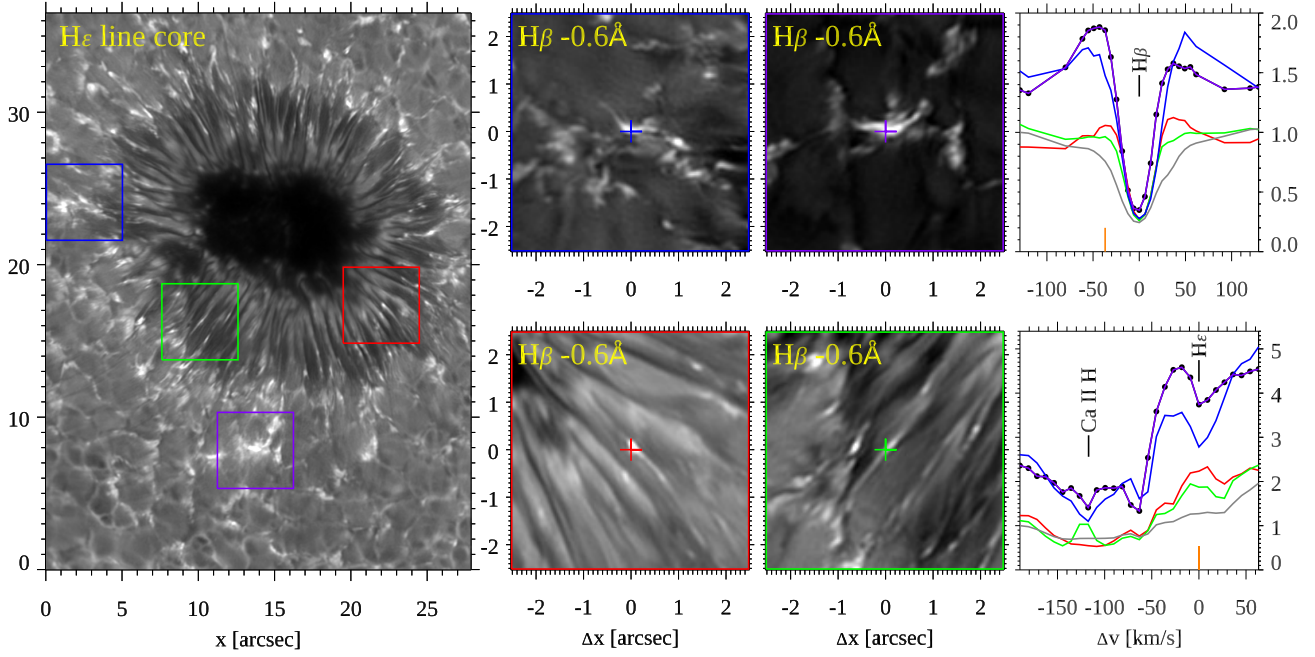


Fig. 3. Ellerman bombs in the sunspot penumbra and around the sunspot in the moat observed on 07 August 2020. The colored squares in the overview H ϵ line core image (left) are centered on EB examples that are shown at higher magnification in the H β wing in the center. The blue and purple line profiles in the spectral plots (right) show the two EBs outside the sunspot. The red and green profiles are PEBs in the penumbra.

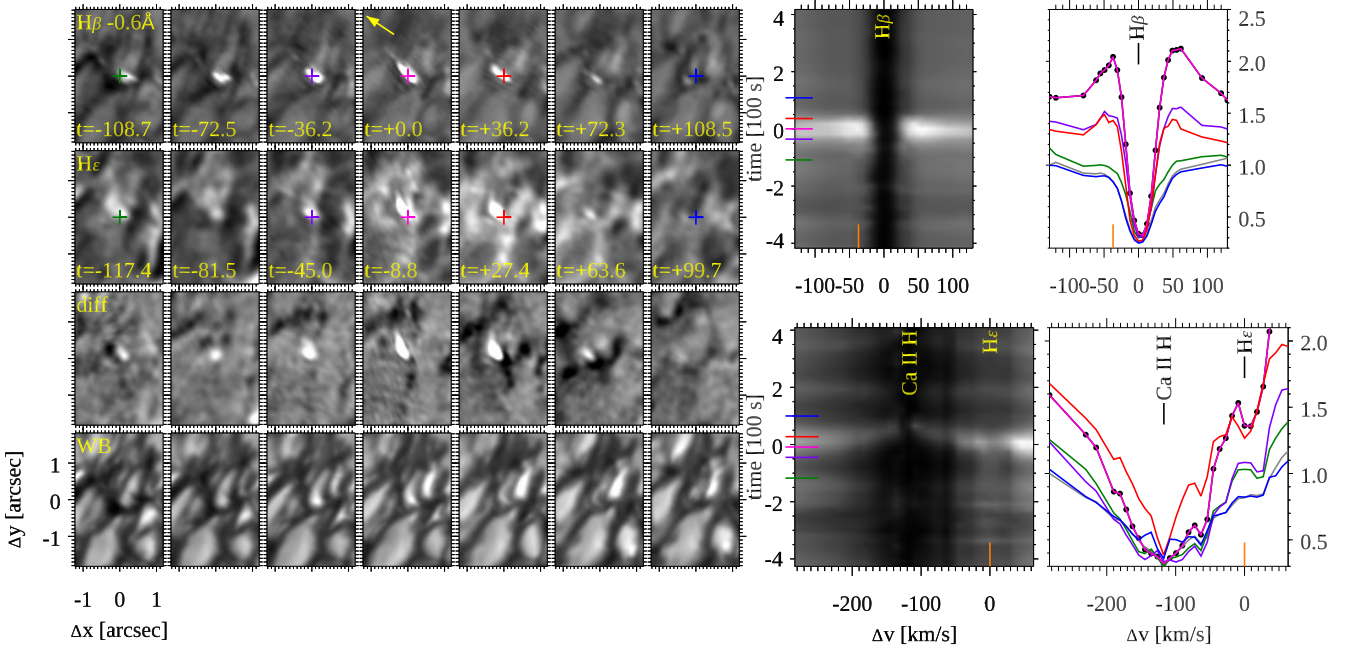


Fig. 4. Temporal evolution of a QSEB observed at $\mu = 0.54$ on 16 August 2020. On the left, a series of small images are centered on a QSEB (from the top to bottom row) in the H β wing, the H ϵ line center, the difference H ϵ - Ca II H blue wing, and WB 4846 Å. The λt diagrams to the right show the spectral evolution at the pixel location marked with a cross in the H β wing and H ϵ images. The colored markers indicate the times for which spectral profiles are shown on the right. An animation of this figure is available [online](#).

Figure 3 shows examples of EBs in and around a sunspot. The EBs in the sunspot moat outside the penumbra are very bright in the H β wing images and have a strongly enhanced intensity in the H β and H ϵ wings. For both EBs, the H ϵ line clearly has enhanced emission compared to the Ca II H blue wing and an absorption feature at H ϵ line center. The EBs in the penumbra, or PEBs, have the characteristic EB spectral line shape in H β , but with a much weaker wing enhancement. The H ϵ

line is in emission for these PEBs, but it is far weaker than the two EB examples in the sunspot moat. There is a hint of a weak absorption feature at the H ϵ line center, but it is not resolved.

Figure 4 shows the temporal evolution of a QSEB in H β and H ϵ . The total lifetime of the QSEB is about 8 min, as can be seen from the associated movie. The spectral profiles in Fig. 4 are taken from a fixed pixel location, and the H β wing intensity increases by more than a factor of 2 as the QSEB moves

through this pixel location. The $H\epsilon$ line evolves from a weak emission feature in the early profiles (green and purple) to a more enhanced feature for the pink and red profiles. It is finally absent in the last blue profile. The $H\epsilon$ line is stronger for the pink and red profiles, but the Ca II H wing is also more enhanced at these times. In the panels that show the difference between $H\epsilon$ and Ca II H wing, the QSEB emission patch is clearly visible. These panels also show that the strongest $H\epsilon$ emission does not arise at the pixel location in which the $H\beta$ wing is strongest. The strongest $H\epsilon$ emission is slightly offset toward the upper left in the limb-ward direction. In the WB 4846 Å images, no trace of the QSEB can be discerned. This confirms the EB characteristic of being invisible in continuum radiation.

4.2. Quiet-Sun Ellerman bomb statistics

The automated detection method we applied to the 16 August 2020 time series allowed us to measure various statistical properties of the QSEBs detected in the two lines. In total, over the full duration of the 24 min time sequence, we detected 961 QSEBs in the $H\beta$ line and 1674 QSEBs in $H\epsilon$. Of these, we found that 561 QSEBs were detected in both lines. Figure 5 presents the distributions of the measured maximum area, lifetime, and maximum brightness of the QSEBs detected in the two lines. The area and brightness are the maximum values over the lifetime of the QSEBs. The format of the figure allows for a direct comparison with the $H\beta$ QSEB statistics in Paper II (their Fig. 6), and we conclude that our distributions are very similar to their data. The mean and median values of the distributions are given in Table 2. The table also includes values from Paper II.

Comparing the distributions between the two lines, we conclude that they are generally very similar. All distributions are positively skewed; the distributions have more weight toward the lower values and a tail toward the higher values. The distribution for the maximum area in $H\epsilon$ is less skewed toward low values than in $H\beta$, meaning that more larger-area QSEBs are visible in $H\epsilon$ (the median maximum area in $H\epsilon$ is 1.5 times larger). The lifetime distributions are very similar, with mean and median values that are almost identical. The values for the maximum brightness are more difficult to compare between the two lines because they are measured differently. The QSEB brightness in $H\epsilon$ is measured against the Ca II H blue wing, while in $H\beta$ it is measured against the average far-wing intensity in the local vicinity (like in Paper II). The maximum brightness in $H\epsilon$ has a sharp cutoff at a minimum value of 1.25. This cutoff was needed because we found that below this value, we obtained many clearly false detections. We attribute these false detections to neighboring spectral line blends that can suggest a weak emission feature in $H\epsilon$. These blends are weak spectral lines from neutral species: Fe I, Cr I, and Ni I.

Figure 5 includes joint probability distribution functions (JPDFs) with scatter plots between the three parameters. As presented in Paper II, both spectral lines show the general trend that QSEBs with a larger maximum area have a longer lifetime and are also brighter. However, the scatter between these parameters is very large. A comparison of the JPDFs that include the maximum area, panels (d) versus (j) and panels (f) versus (l), clearly shows that more QSEBs in $H\epsilon$ are larger.

A subset of the QSEBs was detected in the two spectral lines (561 QSEBs). Figure 6 presents the statistics for the time difference when the QSEB first appeared in the two lines, the distance measured for their centers of gravity, and their orientation. The measurement method was similar to that for QSEBs in Paper II,

who showed both $H\beta$ line core and line wing brightening (see their Fig. 5 for an illustration of the measurement). Most of the QSEBs first appear in $H\beta$ ($\Delta t > 0$), and 21% first appear in $H\epsilon$. All QSEBs have a spatial offset between the two lines, and 8.5% of the QSEBs have a distance d smaller than 200 km. The direction of the offset is mostly in the limb-ward direction. We find that 70% of the QSEBs in $H\epsilon$ are within $\pm 45^\circ$ from their counterpart in $H\beta$. This means that the majority of the $H\epsilon$ QSEBs are closer to the limb. Figure 6c presents the average propagation speed as measured from the distance d and time difference Δt . The propagation speeds are comparable to what was found between the $H\beta$ line core and wing in Paper II: Most speeds are $< 10 \text{ km s}^{-1}$.

To test whether the QSEBs that are detected in both spectral lines are different from the QSEBs that are detected in $H\beta$ alone, Fig. 7 presents the $H\beta$ statistical distributions separately for the two populations. The distributions for the maximum area and brightness are very similar. For the distributions of the lifetimes, more longer-lived QSEBs appear to be detected in both lines. This comparison shows that QSEBs that are detected in both lines are not fundamentally very different from the QSEBs that are detected in the $H\beta$ line alone.

Figure 8 shows four different examples of QSEBs: Two that are detected in both $H\beta$ and $H\epsilon$ and two that are detected in one spectral line alone. The QSEB in panels (a) first appears in $H\beta$ and later in $H\epsilon$. The QSEB in $H\epsilon$ is clearly offset in the limb-ward direction. The temporal evolution suggests an upward propagation speed of about 7 km s^{-1} . In example (b), the QSEB first appears in $H\epsilon$ and later in $H\beta$. There is no clear propagation speed, but the QSEB in $H\epsilon$ is clearly offset in the limb-ward direction. The QSEB in (c) is clearly observed in $H\beta$ but cannot be discerned in $H\epsilon$, while the QSEB in (d) is absent in $H\beta$, but clearly present in $H\epsilon$. In the space-time diagram of example (d), an upward propagation is apparent in the $H\epsilon$ line.

Figure 9 presents the spatial distribution of QSEB detections over the full 24 min time series. QSEBs can be found throughout the FOV, with denser concentrations in areas with a stronger magnetic field. The spatial distribution of the photospheric magnetic field are shown in the top panel of Fig. 9, which shows a map of the extreme values of B_{LOS} . More than 1.7 times more QSEBs are detected in $H\epsilon$ and more than half of the $H\beta$ QSEBs are also detected in $H\epsilon$. The QSEB distribution map is therefore dominated by the blue dots of the $H\epsilon$ detections. The internetwork is also covered by QSEBs, but the map shows small voids with a width of approximately 3–6 mm. This means that in small areas in the FOV, no QSEBs appear during the 24 min duration of the time series. These empty areas are regions with weak magnetic fields with generally $|B_{\text{LOS}}| < 50 \text{ G}$.

Like in Paper II, we marked regions in which for the duration of the time series, both polarities of significant strength ($|B_{\text{LOS}}| > 50 \text{ G}$) are present (blue contours). This illustrates that the occurrence of opposite polarities in close vicinity is very common, and we find QSEBs in and near these regions.

Figure 10 presents the number of QSEB detections in relation to the seeing quality. As was found in Paper II, the number of QSEB detections is clearly correlated with the seeing quality: During the best seeing times, the highest number of QSEBs are detected. The maximum number of QSEB detections is 182. This occurred during a period of excellent seeing when the r_0 peaked up to 50 cm. The highest number of $H\beta$ QSEB detections is 94 (the sum of $H\beta$ only detections and both $H\beta$ and $H\epsilon$ detections). The highest number of $H\epsilon$ detections is 140.

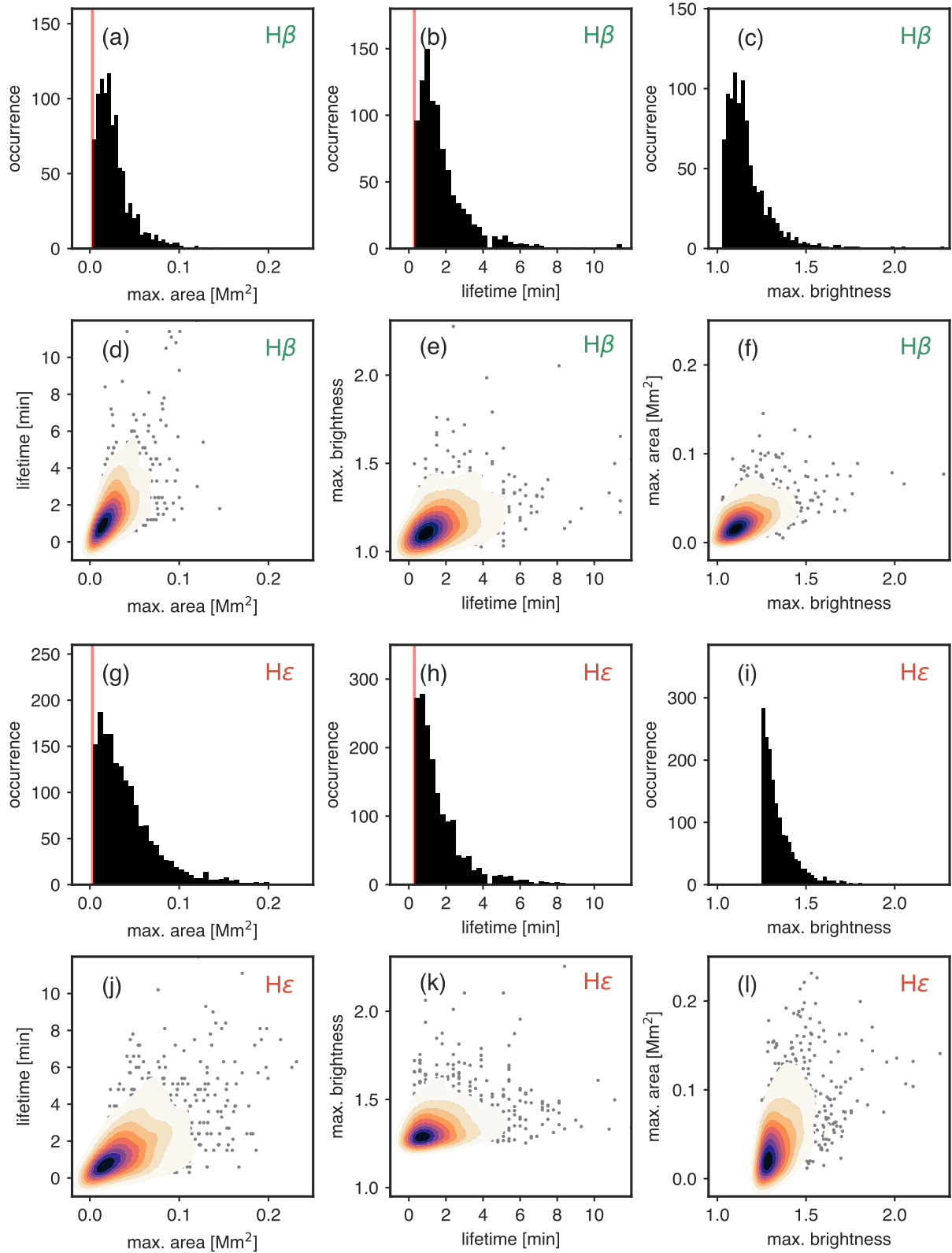


Fig. 5. Statistical properties of QSEBs detected in the 24 min time series on 16 August 2020. The total number of $H\beta$ QSEBs is 961, and the number of $H\epsilon$ QSEBs is 1674. The filled black histograms in panels (a)–(c) and (g)–(i) represent the maximum area, lifetime, and maximum brightness distributions, respectively. The vertical red line marks the lower limit set by the sampling: 0.0008 mm^2 (one pixel) in area (panels (a) and (g)) and 18 s in lifetime (panels (b) and (h)). In panels (d)–(f) and (j)–(l), multivariate JPDFs and scatter plots between the maximum area, lifetime, and maximum brightness are shown. The dark blue shade of the JPDFs indicates where the highest density occurs, and the lighter orange shaded regions represent the low-density distribution.

Table 2. Statistical properties of QSEBs.

	QSEBs in H β (Paper II)		QSEBs in H β		QSEBs in H ϵ	
	Mean	Median	Mean	Median	Mean	Median
Max. area [mm ²] (pixels) ^(a)	0.0277 (36)	0.0203 (26)	0.0270 (36)	0.0222 (30)	0.0433 (58)	0.0334 (45)
Lifetime [min] (frames) ^(a)	1.65 (11)	1.14 (8)	1.80 (6)	1.20 (4)	1.62 (5)	1.20 (4)
Max. brightness	1.28	1.22	1.17	1.14	1.35	1.31

Notes. ^(a)The values in parentheses are the nearest integer numbers.

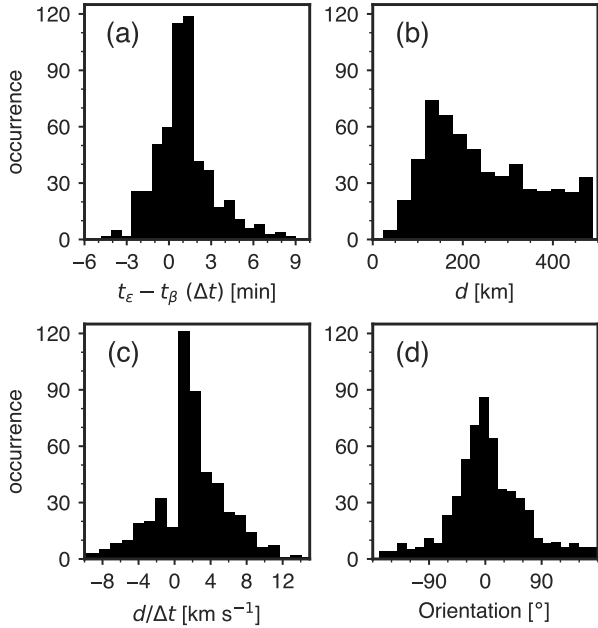


Fig. 6. Time difference, distance, average propagation speed, and orientation of the brightening of QSEBs in H ϵ with respect to their counterparts in H β . Measurements are based on the first appearance of the QSEB in the respective spectral line. Positive values of the propagation speed $d/\Delta t$ imply that the QSEB first occurred in H β . The orientation angle is measured against the direction toward the closest limb. An orientation of 0° means that the QSEB in H ϵ is closer to the limb than the QSEB measured in H β . The total number of QSEBs measured in both H ϵ and H β is 561.

5. Discussion

We used high-quality observations to analyze EBs in the H ϵ line and compared them with cotemporal H β and H α observations. We conclude that the H ϵ line is well suited for studying the EB phenomenon: It shows a similar morphology and dynamics as in the traditional Balmer lines, with the advantage of a higher spatial resolution due to its shorter wavelength. This means that magnetic reconnection might be probed at a very small spatial scale.

In a textbook EB in an active region that occurred as the result of the coalescence of opposite magnetic-polarity patches after a strong magnetic flux emergence, we found that the flame-like morphology and rapid variability were similar in the H ϵ line to those in H β . In a small active region close to the limb, a tall and thin EB flame is visible in both H ϵ and H β . The H ϵ line is clearly enhanced, and for the observations with extended Ca II H blue-wing coverage, the H ϵ line is clearly higher than the Ca II H wing. In the penumbra of a sunspot, we find that the PEB emission in H ϵ is not as high as for EBs outside the sunspot. Still, the

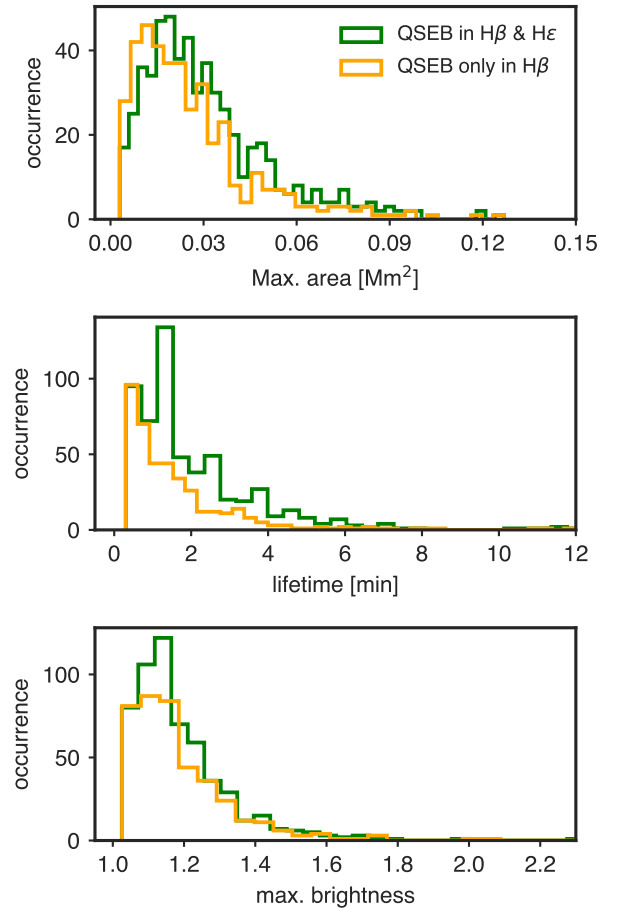


Fig. 7. Comparison of the statistical properties measured in H β between QSEB events detected in the H β and H ϵ lines and those that are only found in the H β line. The total number of QSEBs detected in both H ϵ and H β is 561. The total number of QSEBs detected in H β alone is 400.

H ϵ line is a clear emission feature. Weak H ϵ emission lines can effectively be identified by subtraction of the opposite Ca II H blue wing. For our quiet-Sun observations, this was an effective method for identifying QSEBs.

In a 24 min time series, we detected 1674 QSEBs in H ϵ and 961 QSEBs in H β . A subset of these, 561 QSEBs, were detected in both spectral lines (almost 60% of the H β QSEBs). We found that the QSEB characteristics measured in H ϵ are not fundamentally different from the measurements in H β . The lifetime measurements are very similar. The QSEBs in H ϵ appear to be somewhat larger: The median of the maximum area distribution is 1.5 times larger in H ϵ . The spatial distribution of QSEBs in H ϵ is similar to that in H β . In both lines, QSEBs are detected throughout the FOV, with denser concentrations in the network areas.

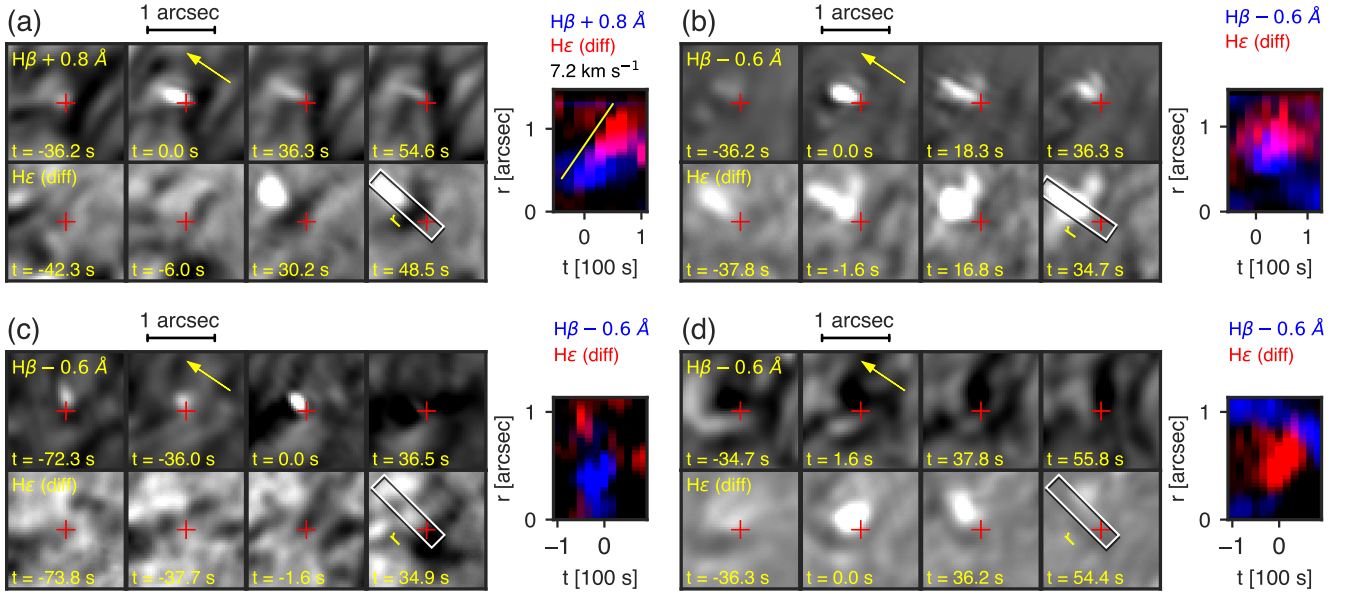


Fig. 8. Examples of the temporal evolution of QSEBs. (a) QSEB first observed in $H\beta$ and then in $H\epsilon$. (b) QSEB first observed in $H\epsilon$ and then in $H\beta$. (c) QSEB observed in $H\beta$ alone. (d) QSEB observed in $H\epsilon$ alone. The bottom row of images shows difference ($H\epsilon - \text{Ca II H blue wing}$) images. White shows emission in $H\epsilon$. Each image is scaled individually. The bottom right panels show a rectangular box along which a space-time diagram along the distance r is shown in the right panels. The yellow arrows indicate the direction toward the limb, so that $r = 1$ is closer to the limb.

Similar to our findings in Paper II, small voids with a width of 3–6 mm were observed, in which no QSEBs were detected. These voids are evenly distributed over the FOV, are generally regions with a weak magnetic field, and recall the mesogranular pattern. The majority of QSEBs are found in the vicinity of magnetic field concentrations. Most regions that have both magnetic polarities in close proximity also have QSEBs. This supports the interpretation that QSEBs are effective markers of magnetic reconnection.

We detected 961 $H\beta$ QSEBs in the 24 min time series, and in Paper II, we found 2809 QSEBs in a 60 min time series from 2019. With a simple correction for the shorter duration, we see that we found 15% fewer QSEBs in the 2020 data set. Some differences between the two data sets might contribute to the lower detection number: In this 2020 data set, the two-line program resulted in a temporal cadence almost twice as high as that of the 2019 data. The faster-cadence 2019 data allowed us to detect more short-lived QSEBs. Furthermore, there are differences in the seeing quality. In Paper II, we found a clear positive correlation between the seeing quality and the number of QSEB detections, which we also found here (see Fig. 10). Both data sets have a high image quality, but the 2019 r_0 values for the full atmosphere are higher than the 2020 values for 14% of the time steps (i.e., 59 time steps have $r_0 > 13$ cm). More QSEBs could be detected in the 2019 data because more time steps had excellent seeing. Another difference is the observing angle: The 2020 data lie $192''$ further away from the disk center, and there is a 17° difference in observing angle. The solar photosphere is not a plane surface, and the $\tau = 1$ surface can be described as a corrugated landscape with granular hills and intergranular valleys. One possible effect of different observing angles is that some small QSEBs that reside in the intergranular lanes could be hidden behind granules in the foreground in the 2020 data. Finally, there could be a difference in the number of QSEBs caused by the intrinsic differences between the two regions.

We detected significantly more QSEBs in $H\epsilon$ than in $H\beta$ (1.7 times more in $H\epsilon$). During the best seeing moments, we detected up to 182 QSEBs (i.e., the sum of QSEBs detected in $H\epsilon$ alone, in $H\beta$ alone, and detected in both $H\epsilon$ and $H\beta$). This means more QSEB detections by about a factor 1.5 times than in Paper I and Paper II. There, from a rough extrapolation of the highest detection number and the observation area, it was estimated that at as many as 500 000 QSEBs might be present on the solar surface at any given time. The higher number of QSEB detections in $H\epsilon$ we find here suggests that this estimate can be increased to 750 000 QSEBs. We consider this a conservative increase in the estimate: For the reasons discussed in the previous paragraph, it is likely that a considerable larger number of QSEBs can be detected with a more dedicated $H\epsilon$ observation program with a faster temporal cadence and with better seeing conditions.

The formation of the traditional Balmer series lines such as $H\alpha$ and $H\beta$ differs significantly from the formation of $H\epsilon$ in the solar atmosphere (Krikova et al. 2023). $H\epsilon$ is formed relative to the strong Ca II H wing, whereas $H\alpha$ and $H\beta$ are formed relative to the solar continuum. The Ca II H wing intensity at the $H\epsilon$ wavelength shows a reversed granulation intensity pattern that is formed higher in the atmosphere than the solar optical continuum radiation. For $H\epsilon$, the deepest we can view into the solar atmosphere is the reversed granulation layer. This is a height of about 300 km above the surface in the simulation analyzed by Krikova et al. (2023). For $H\alpha$ and $H\beta$, the deepest we can view is the solar photosphere, represented by granulation observed in the line wings. This could explain the limb-ward spatial offset between EB observations in $H\beta$ and $H\epsilon$, as $H\epsilon$ does not observe the EB structure below the reversed granulation layer. This may further serve as one of the explanations of why some QSEBs are detected in $H\beta$ alone and some in $H\epsilon$ alone: The QSEBs that occur deepest in the atmosphere may not be observable in $H\epsilon$. QSEBs that occur higher in the atmosphere may not be observable in the $H\beta$ wing, but may still be present in the $H\epsilon$ core. The time difference of many QSEBs that are first detected in

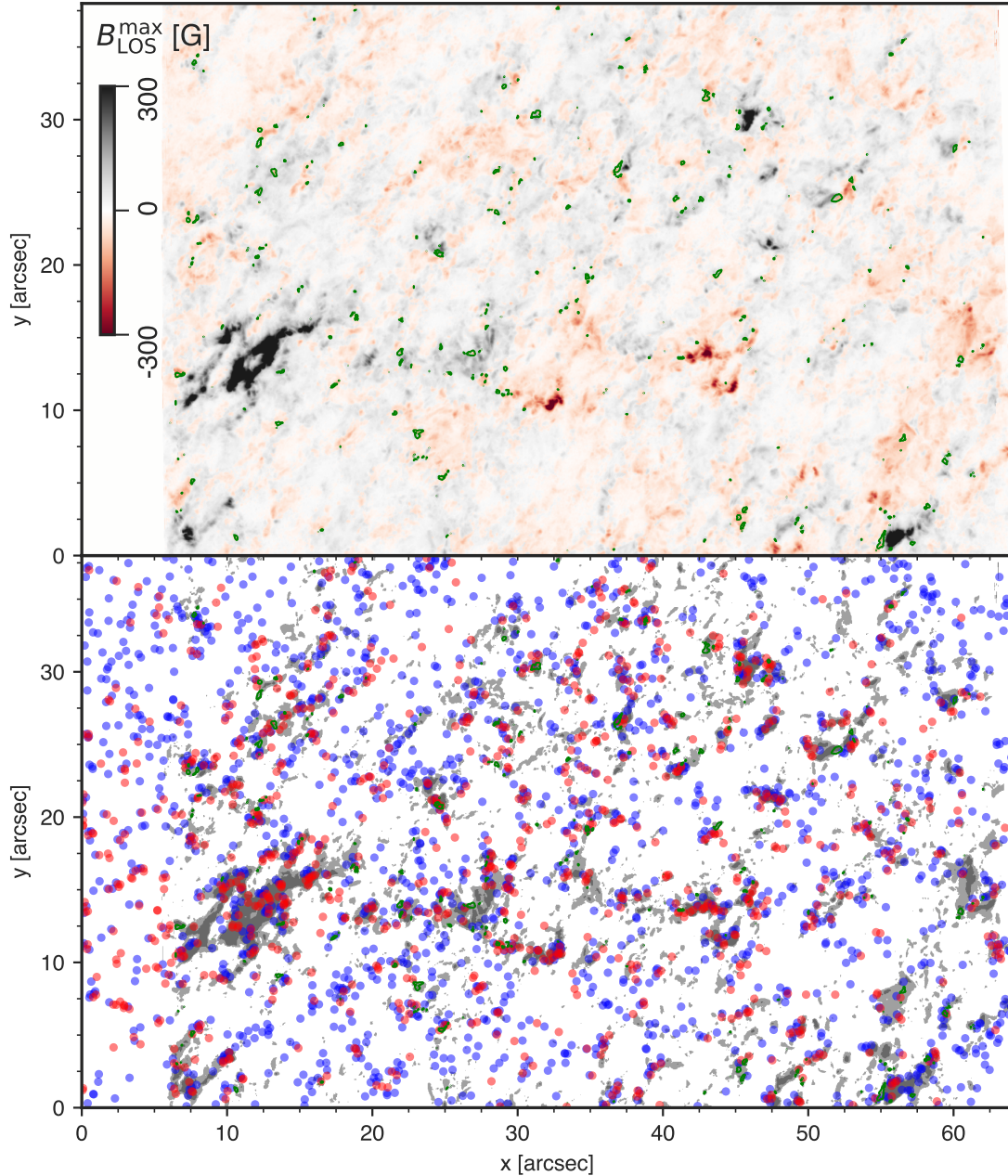


Fig. 9. Spatial distribution of QSEBs and their magnetic environment. The top panel shows at each pixel the extremum of B_{LOS} over the full 24 min duration of the time series. Green contours mark pixels that have $|B_{\text{LOS}}| > 50$ G for both polarities during the time series. The bottom panel shows QSEB detections in $\text{H}\beta$ (red) and $\text{H}\epsilon$ (blue). There are 961 QSEBs in $\text{H}\beta$ and 1674 QSEBs in $\text{H}\epsilon$. The shaded background marks regions where $|B_{\text{LOS}}^{\text{max}}| > 100$ G (dark gray) and $50 < |B_{\text{LOS}}^{\text{max}}| < 100$ G (light gray). The CRISP FOV is slightly narrower than for CHROMIS, so that the region for $x < 6''$ is not covered by the magnetic field map.

$\text{H}\beta$ and later in $\text{H}\epsilon$ suggests that magnetic reconnection often first starts deep in the atmosphere and propagates upward in the atmosphere. Our measurements indicate that the typical propagation speed is below 10 km s^{-1} . We find that about one-fifth of the QSEBs first occur in $\text{H}\epsilon$. This suggests that in some events, reconnection starts higher in the atmosphere and propagates downward. These findings are consistent with the time differences and propagation speeds measured between the $\text{H}\beta$ wing and core in Paper II. We find that the maximum area of QSEBs detected in $\text{H}\epsilon$ is larger than in $\text{H}\beta$ on average. This might be related to the higher formation height in $\text{H}\epsilon$, and we see the effect of magnetic structures that fan out to a larger area with increasing height.

Other factors might contribute to some QSEBs being detected in only one of the spectral lines. QSEBs evolve on very short timescales, and some may have already decayed below the detection limit by the time the CHROMIS instrument was tuned to the other spectral line. Seeing variations are another factor for some of the nondetections. Furthermore, some weak emission in the other spectral line might in fact be present, but may not pass the thresholds of our detection method. We manually inspected a number of single-line QSEB detections and found weak QSEB features in the other spectral line.

Most of the presented $\text{H}\epsilon$ EB spectral profiles show a weak absorption dip in addition to the larger emission feature. These weak absorption features imply that a part of the observed

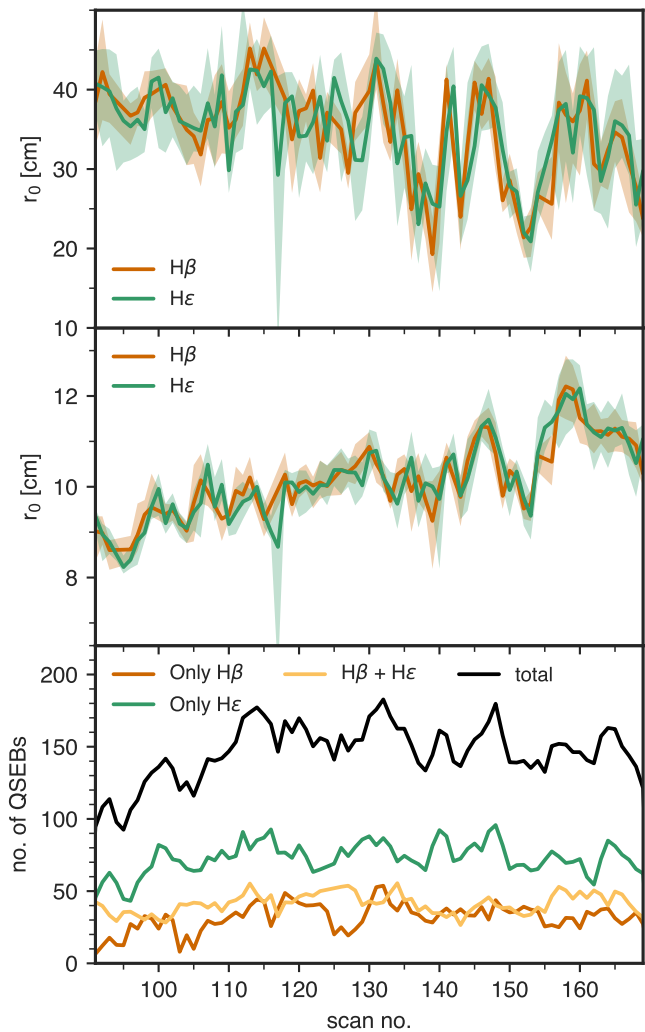


Fig. 10. Impact of the seeing quality on the number of QSEB detections. The top two panels show the Fried parameter r_0 as a function of time (indicated as the scan number in the 24 min time series, which started at 90). The top panel shows r_0 values that are a measure of the ground-layer seeing alone. The middle panel shows r_0 values that measure the seeing over the whole atmosphere. The $H\beta$ and $H\epsilon$ lines were recorded sequentially, so there are two separate curves for the two spectral lines. The solid curves show the average r_0 values during the scan, and the shaded area shows the range of r_0 values during the spectral scan. The bottom panel shows the number of QSEB detections per scan differentiated by QSEBs detected in $H\beta$ alone, in $H\epsilon$ alone, or in both $H\beta$ and $H\epsilon$. The black curve shows the total number of QSEB detections as the sum of these three curves.

intensity comes from atmospheric layers above the EB reconnection site. We observe the same morphological EB structures in the line core as in the wing of $H\epsilon$. This means that the layers above EBs are not optically thick enough to fully block the radiation from the EB, and the absorption dip is formed under optically thin conditions. This is different for the $H\alpha$ and $H\beta$ lines: Both lines show chromospheric structures in the line core, and the chromospheric fibrils are optically thick to $H\alpha$ and (to somewhat lesser extent) $H\beta$ line core radiation from the EB site below. The fact that the chromosphere is optically thin in $H\epsilon$ can be seen in the $H\epsilon$ line core images in Fig. 3, and in Fig. 1 in Krikova et al. (2023): these images show a scene that is dominated by the Ca II H wing and shows mostly inverse granulation. Only under larger magnification can some signature of thin chromospheric fibrils be discerned

in certain areas. These are the darkest fibrils in cotemporal $H\alpha$ or $H\beta$ line core images. This is also illustrated by the animation of the spectral line scan in Fig. 1.

We have demonstrated that the $H\epsilon$ line is well suited as a diagnostic of EBs. With its short wavelength, it arguably allows for observations with the highest spatial resolution of magnetic reconnection in the solar atmosphere. This is of particular interest as a science case for the 4 m DKIST telescope (Rimmele et al. 2020), the upcoming EST telescope (Quintero Noda et al. 2022), and the third launch of the balloon-borne Sunrise observatory (Solanki et al. 2010), which with its SUSI spectropolarimeter (Feller et al. 2020) has access to multiple short-wavelength Balmer lines between 300 and 410 nm.

Acknowledgements. The Swedish 1-m Solar Telescope is operated on the island of La Palma by the Institute for Solar Physics of Stockholm University in the Spanish Observatorio del Roque de los Muchachos of the Instituto de Astrofísica de Canarias. The Institute for Solar Physics is supported by a grant for research infrastructures of national importance from the Swedish Research Council (registration number 2017-00625). This research is supported by the Research Council of Norway, project numbers 250810, 325491, and through its Centres of Excellence scheme, project number 262622. K.K. acknowledges funding support by the European Research Council under ERC Synergy grant agreement No. 810218 (Whole Sun). J.J. is grateful for travel support under the International Rosseland Visitor Programme. We are most grateful to Pit Sütterlin for his outstanding work to acquire the SST observations in service mode when international travel was impossible due to COVID19 restrictions and it was impossible for us to come to the telescope. We made much use of NASA's Astrophysics Data System Bibliographic Services.

References

- Arthur, D., & Vassilvitskii, S. 2007, *Proceedings of the Eighteenth Annual ACM-SIAM Symposium on Discrete Algorithms* (Society for Industrial and Applied Mathematics), 1027
- Bose, S., Nóbrega-Siverio, D., De Pontieu, B., & Roupe van der Voort, L. 2023, *ApJ*, **944**, 171
- Danilovic, S. 2017, *A&A*, **601**, A122
- de la Cruz Rodríguez, J. 2019, *A&A*, **631**, A153
- de la Cruz Rodríguez, J., Löfdahl, M. G., Sütterlin, P., Hillberg, T., & Roupe van der Voort, L. 2015, *A&A*, **573**, A40
- Ellerman, F. 1917, *ApJ*, **46**, 298
- Everitt, B. S. 1972, *Br. J. Psychiatry*, **120**, 143
- Faber, J. T. 2022, Master's Thesis, University of Oslo, Norway
- Fang, C., Tang, Y. H., Xu, Z., Ding, M. D., & Chen, P. F. 2006, *ApJ*, **643**, 1325
- Feller, A., Gandorfer, A., Iglesias, F. A., et al. 2020, *SPIE Conf. Ser.*, **11447**, 8
- Fiorio, C., & Gustedt, J. 1996, *Theor. Comput. Sci.*, **154**, 165
- Georgoulis, M. K., Rust, D. M., Bernasconi, P. N., & Schmieder, B. 2002, *ApJ*, **575**, 506
- Guglielmino, S. L., Bellot Rubio, L. R., Zuccarello, F., et al. 2010, *ApJ*, **724**, 1083
- Hansteen, V. H., Archontis, V., Pereira, T. M. D., et al. 2017, *ApJ*, **839**, 22
- Hansteen, V., Ortiz, A., Archontis, V., et al. 2019, *A&A*, **626**, A33
- Joshi, J., & Roupe van der Voort, L. H. M. 2022, *A&A*, **664**, A72
- Joshi, J., Roupe van der Voort, L. H. M., & de la Cruz Rodríguez, J. 2020, *A&A*, **641**, L5
- Krikova, K., Pereira, T. M. D., & Roupe van der Voort, L. H. M. 2023, *A&A*, **677**, A52
- Löfdahl, M. G., Hillberg, T., de la Cruz Rodríguez, J., et al. 2021, *A&A*, **653**, A68
- Matsumoto, T., Kitai, R., Shibata, K., et al. 2008, *PASJ*, **60**, 577
- Nelson, C. J., Shelyag, S., Mathioudakis, M., et al. 2013, *ApJ*, **779**, 125
- Nelson, C. J., Scullion, E. M., Doyle, J. G., Freij, N., & Erdélyi, R. 2015, *ApJ*, **798**, 19
- Nelson, C. J., Freij, N., Reid, A., et al. 2017, *ApJ*, **845**, 16
- Pariat, E., Aulanier, G., Schmieder, B., et al. 2004, *ApJ*, **614**, 1099
- Pariat, E., Schmieder, B., Berlicki, A., et al. 2007, *A&A*, **473**, 279
- Quintero Noda, C., Schlichenmaier, R., Bellot Rubio, L. R., et al. 2022, *A&A*, **666**, A21
- Reid, A., Mathioudakis, M., Doyle, J. G., et al. 2016, *ApJ*, **823**, 110
- Rimmele, T. R., Warner, M., Keil, S. L., et al. 2020, *Sol. Phys.*, **295**, 172

- Roupe van der Voort, L. H. M., Rutten, R. J., & Vissers, G. J. M. 2016, [A&A](#), **592**, [A100](#)
- Roupe van der Voort, L., De Pontieu, B., Scharmer, G. B., et al. 2017, [ApJ](#), **851**, [L6](#)
- Roupe van der Voort, L. H. M., Joshi, J., Henriques, V. M. J., & Bose, S. 2021, [A&A](#), **648**, [A54](#)
- Roupe van der Voort, L. H. M., van Noort, M., & de la Cruz Rodríguez, J. 2023, [A&A](#), **673**, [A11](#)
- Rutten, R. J., Vissers, G. J. M., Roupe van der Voort, L. H. M., Sütterlin, P., & Vitas, N. 2013, [J. Phys. Conf. Ser.](#), **440**, [012007](#)
- Scharmer, G. B., Bjelksjö, K., Korhonen, T. K., Lindberg, B., & Petterson, B. 2003, in *Innovative Telescopes and Instrumentation for Solar Astrophysics*, eds. S. L. Keil, & S. V. Avakyan, [Proc. SPIE](#), **4853**, [341](#)
- Scharmer, G. B., Löfdahl, M. G., Sliepen, G., & de la Cruz Rodríguez, J. 2019, [A&A](#), **626**, [A55](#)
- Scharmer, G. B., Narayan, G., Hillberg, T., et al. 2008, [ApJ](#), **689**, [L69](#)
- Severny, A. B. 1964, [ARA&A](#), **2**, [363](#)
- Shetye, J., Shelyag, S., Reid, A. L., et al. 2018, [MNRAS](#), **479**, [3274](#)
- Solanki, S. K., Barthol, P., Danilovic, S., et al. 2010, [ApJ](#), **723**, [L127](#)
- van Noort, M., Roupe van der Voort, L., & Löfdahl, M. G. 2005, [Sol. Phys.](#), **228**, [191](#)
- Vissers, G. J. M., Roupe van der Voort, L. H. M., & Rutten, R. J. 2013, [ApJ](#), **774**, [32](#)
- Watanabe, H., Kitai, R., Okamoto, K., et al. 2008, [ApJ](#), **684**, [736](#)
- Watanabe, H., Vissers, G., Kitai, R., Roupe van der Voort, L., & Rutten, R. J. 2011, [ApJ](#), **736**, [71](#)

Appendix A: k -means clustering and QSEB detections

Figures A.1 and A.2 show the RPs from the k -means clustering of the $H\beta$ and $H\epsilon$ lines that are identified as a signature of QSEB. The clustering was made for 81 time steps of the 16 August 2020 quiet-Sun data with 1686×1000 pixels per time step. We used 100 clusters for the clustering of the $H\beta$ and $H\epsilon$ spectra. The $H\beta$ QSEB clusters in Fig. A.1 were differentiated into three groups following Paper II. The blue clusters (RPs 0–9) are the characteristic EB profiles with significantly enhanced wings and a largely unaffected line core. Each $H\beta$ QSEB event is required to have profiles from these clusters. Pixels with profiles from the green (RPs 10–12, weakly enhanced wings) or red clusters (RPs 13 and 14, enhanced line core) were added to the event when they were connected in space and time to the pixels with blue cluster profiles. More details about the detection of $H\beta$ QSEBs are provided in Paper II.

Figure A.3 illustrates the procedure for connecting $H\beta$ and $H\epsilon$ QSEB detections in time. For all four cases, we assumed that

the $H\beta$ and $H\epsilon$ detections are connected in space: The centroids of all pairs are separated by less than 500 km. In panel (a), the $H\beta$ QSEB detection starts before the $H\epsilon$ detection, but the $H\epsilon$ detection starts before the $H\beta$ detection ends ($t_{\text{start}}(H\epsilon) < t_{\text{end}}(H\beta)$). The QSEB is detected for at least one time step in both $H\beta$ and $H\epsilon$, so this is a clearly connected QSEB. The case in panel (b) is also a clearly connected QSEB because the later $H\beta$ QSEB detection starts before the end of the $H\epsilon$ detection. For the cases in panels (c) and (d), there is a time gap between the QSEB detections: The $H\beta$ and $H\epsilon$ detections are close in time, but do not share a common time step. The maximum allowed time gap was nine time steps or 162 s (i.e., for (c): $t_{\text{start}}(H\epsilon) - t_{\text{end}}(H\beta) \leq 162$ s and for (d): $t_{\text{start}}(H\beta) - t_{\text{end}}(H\epsilon) \leq 162$ s).

The 500 km threshold for a spatial connection was found to be a reasonable limit to avoid many ambiguous connections. By varying the spatial distance threshold, we found that for larger distances above 500 km, the number of connected events increased rapidly and the statistical distributions for orientation and time difference in Fig. 6 changed significantly.

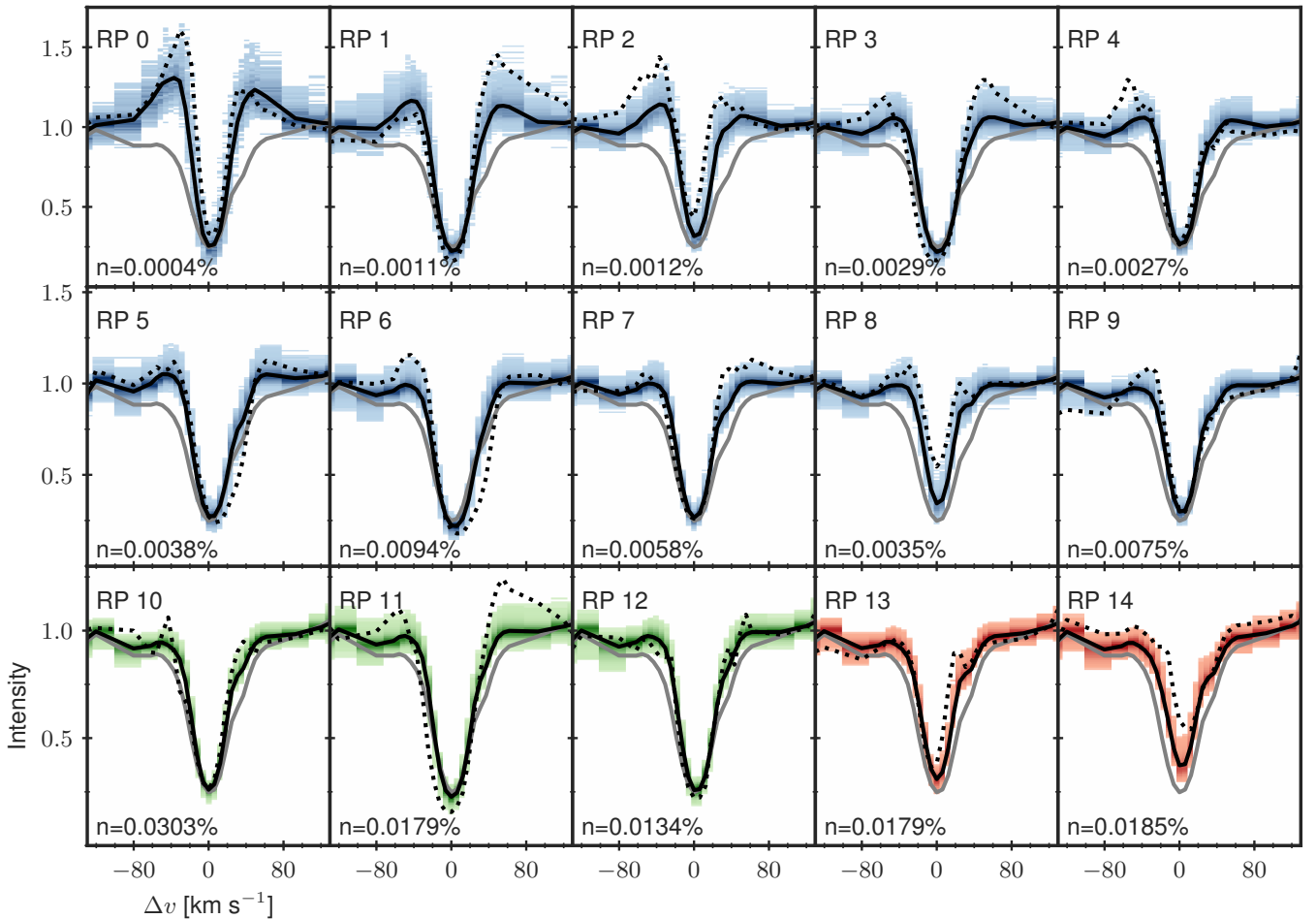


Fig. A.1. Fifteen RPs from the k -means clustering of the $H\beta$ line that are identified as a signature of QSEB. The black lines show RPs, and shaded colored areas represent the density distribution of $H\beta$ spectra within a cluster. Darker shades indicate a higher density. Within a particular cluster, the $H\beta$ profile that is farthest (measured in Euclidean distance) from the corresponding RPs is shown by the dotted black line. As reference, the average quiet-Sun profile (gray line) is plotted in each panel. RPs 0–9 (blue) show the typical EB-like $H\beta$ profiles, i.e., significantly enhanced wings and an unaffected line core, while RPs 10–12 (green) display weak enhancement in the wings. RPs 13 and 14 (red) show intensity enhancement in the line core. The differentiation into three groups of QSEB clusters is similar as in Paper II. The parameter n represents the number of spectral profiles in a cluster as the percentage of the total of $\sim 1.7 \times 10^9$ spectra.

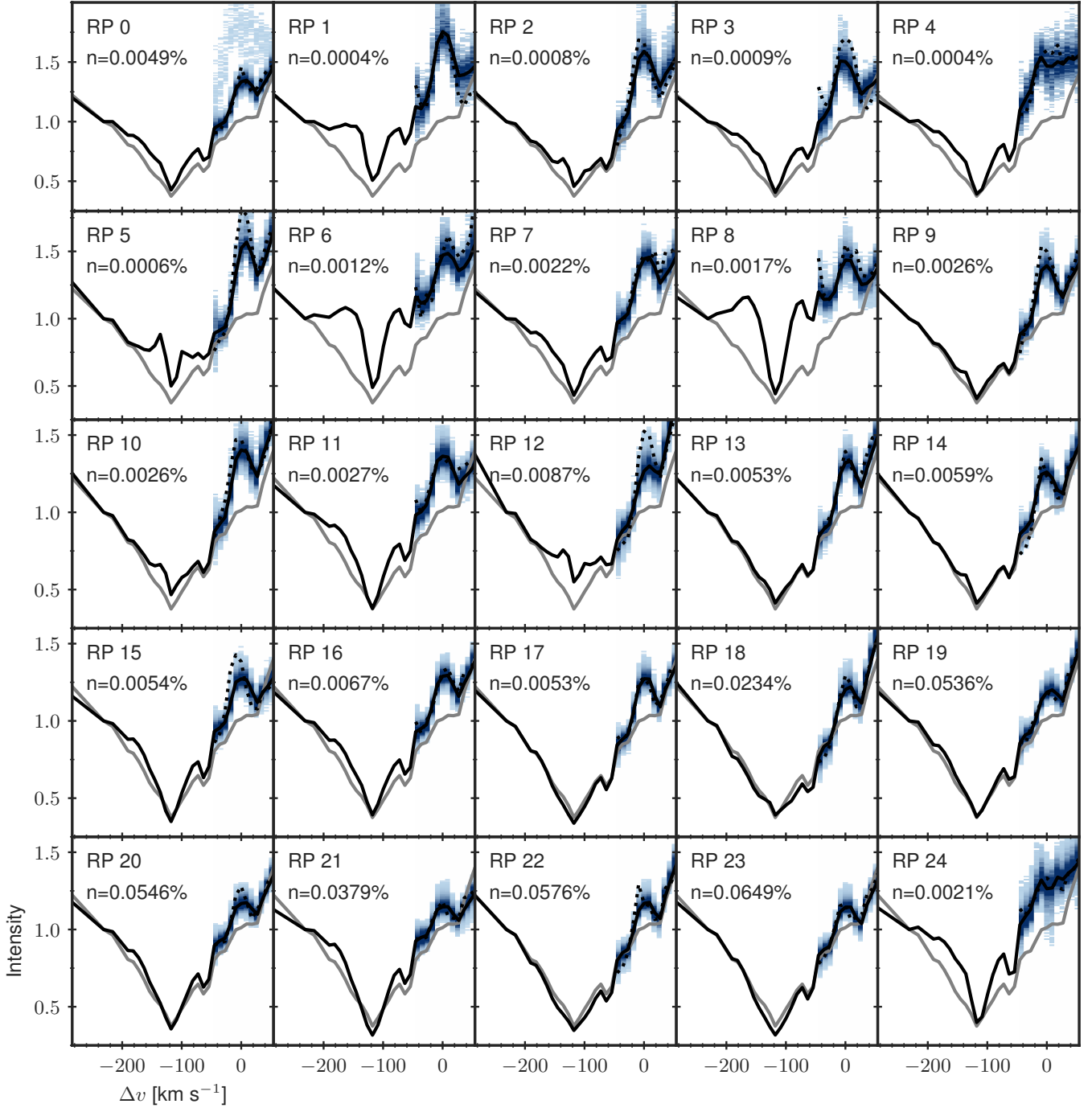


Fig. A.2. Twenty-five RPs (solid black lines) from the k -means clustering of the $H\epsilon$ line that are identified as a signature of QSEB. The k -means clustering was performed for 13 line positions around the $H\epsilon$ nominal line core. The shaded colored areas represent the density distribution of $H\epsilon$ spectra within a cluster. The dotted black line shows the $H\epsilon$ profile that is farthest (measured in Euclidean distance) from the corresponding RP within a particular cluster. The average quiet-Sun profile (gray line) is plotted in each panel as reference. The parameter n represents the number of spectral profiles in a cluster as the percentage of the total of $\sim 1.7 \times 10^9$ spectra.

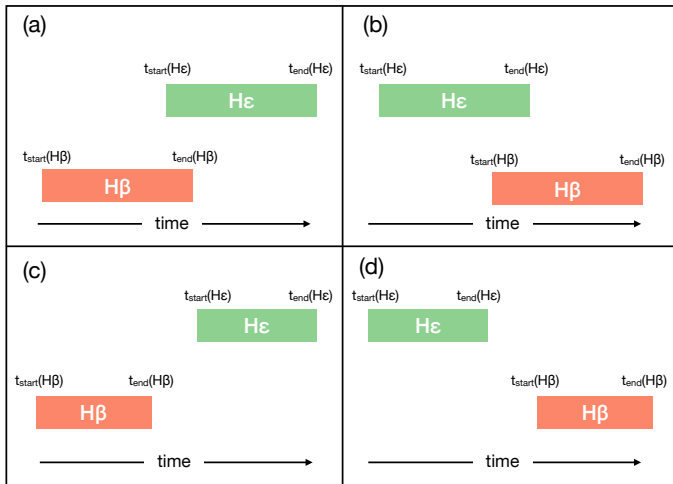


Fig. A.3. Connecting H β and H ϵ QSEB detections in time. Four different cases are shown, and the duration of a QSEB detection is illustrated with colored bars. The spatial connection is not illustrated, but we assumed that the H β and H ϵ detections are spatially connected. The cases in panel (a) and (b) overlap temporally and are therefore clearly temporally connected. The cases in panels (c) and (d) have a time gap between the detections and need to satisfy a temporal condition in order to be considered a connected event.